Flow to Nishimori universality in weakly monitored quantum circuits with qubit loss

Malte Pütz,[1] Romain Vasseur,[2] Andreas W.W. Ludwig,[3] Simon Trebst,[1] and Guo-Yi Zhu[4,*]

[1]*Institute for Theoretical Physics, University of Cologne, Zülpicher Straße 77, 50937 Cologne, Germany*
[2]*Department of Theoretical Physics, University of Geneva, 24 quai Ernest-Ansermet, 1211 Genève, Switzerland*
[3]*Department of Physics, University of California, Santa Barbara, California 93106, USA*
[4]*The Hong Kong University of Science and Technology (Guangzhou), Nansha, Guangzhou, 511400, Guangdong, China*

(Dated: May 30, 2025)

In circuit-based quantum state preparation, qubit loss and coherent errors are circuit imperfections that imperil the formation of long-range entanglement beyond a certain threshold. The critical theory at the threshold is a continuous entanglement transition known to be described by a (2+0)-dimensional non-unitary conformal field theory which, for the two types of imperfections of certain circuits, is described by either percolation or Nishimori criticality, respectively. Here we study the threshold behavior when the two types of errors *simultaneously* occur and show that, when moving away from the Clifford-regime of projective stabilizer measurements, the percolation critical point becomes unstable and the critical theory flows to Nishimori universality. We track this critical renormalization group (RG) crossover flow by mapping out the entanglement phase diagrams, parametrized by the probability and strength of random weak measurements, of two dual protocols preparing surface code or GHZ-class cat states from a parent cluster state via constant-depth circuits. Extensive numerical simulations, using hybrid Gaussian fermion and tensor network / Monte Carlo sampling techniques on systems with more than a million qubits, demonstrate that an infinitesimal deviation from the Clifford regime leads to a sudden, strongly non-monotonic entanglement growth at the incipient non-unitary RG flow. We argue that spectra of scaling dimensions of both the percolation and Nishimori fixed points exhibit *multifractality*. For percolation, we provide the exact (non-quadratic) multifractal spectrum of exponents, while for the Nishimori fixed point we show high-precision numerical results for five leading exponents characterizing multifractality.

Despite the fragility of individual qubits to the effects of leakage, measurement and decoherence, quantum information stored in many physical qubits can be remarkably robust. The surface code, in which long-range many-qubit entanglement protects a single logical qubit, is the quintessential embodiment of this idea and has become a principal design element for fault-tolerant quantum computing architectures. In quantitative terms, the robustness is given by a threshold value that often separates a "correctable" from an "incorrectable" regime and which has been determined for various types of incoherent [1] and coherent [2] noise channels as well as qubit loss [3–6]. These thresholds, however, extend beyond the realm of quantum error correction codes and, taking the example of qubit loss (also known as erasure, leakage or heralded noise), can also be studied to discuss the stability of measurement-based quantum computation [7], photonic quantum computing [8], or open quantum dynamics [9]. But while the numerical value of the threshold might vary for these various settings, they share the commonality that the underlying noisy protocols often fall into the Clifford regime, which allows for an efficient classical numerical computation of the critical threshold. The critical theory at the threshold, however, will depend on the specifics of the noise channel. For qubit loss, the fundamental phase transition is intrinsically linked to the *percolation problem*, a staple of classical statistical mechanics [10]. From a field theoretical perspective, the percolation transition is, in a sense, the simplest, best-understood, and also analytically most tractable example of disorder-induced criticality described by a non-unitary conformal field theory (CFT) [11–15].

In recent times, with interest shifting to critical phenomena in entangled states of matter subject to measurement-induced randomness and non-equilibrium phase transitions in monitored quantum systems [16, 17], percolation again serves not only as the simplest instance of such phenomena [18–20], but also describes [21, 22] the tractable limit (at infinite on-site Hilbert space dimension) of a generic such transition. Percolation belongs to the class of Clifford quantum systems [23], and is special even in this class as it can be described [18–20] as a quantum system of non-interacting fermions [24], monitored by projective measurements. As such, it represents one of the simplest examples in which to study the question of effects of *non-Clifford* perturbations of monitored stabilizer quantum systems. These questions have been the driving motivation for the study reported in this manuscript.

In a quantum circuit, non-Clifford perturbations of even the smallest scale (such as, say, an imperfect $\pi/4$ qubit rotation) drastically change the system – they immediately allow the system's wavefunction to spread into a broader Hilbert space, while at the same time leading to an explicit violation of the Gottesman-Knill condition for classical simulability [25]. Due to these fundamental changes caused by non-Clifford perturbations, the latter are clearly expected to induce a change in critical behavior, a fact that is well established in the context of generic quantum circuits in the above mentioned limit of large on-site Hilbert space dimension [21]. While the latter example provides a 'proof of concept', in the present work we are interested in more 'practical' manifestations of these effects. In fact, all of the currently available quantum circuit platforms do not implement pristine Clifford gates but exhibit a (small) level of imperfections (lending to their classification as noisy intermediate-scale quantum (NISQ) devices), making it a pressing question whether the threshold behavior they

* guoyizhu@hkust-gz.edu.cn

exhibit is dominated by percolation or some other universality class(es).

In this manuscript, we study the effect of non-Clifford perturbations on the percolation transition induced by qubit loss by adding a second noise channel that is known to give rise to distinct critical behavior – Nishimori physics, induced by weak (stabilizer) measurements that give rise to a (tunable) coherent error [2, 26–28]. Putting these two noise channels into direct competition yields a two-dimensional phase diagram where the two critical theories are connected via a line of thresholds, as depicted in Fig. 1. Our key result is that, upon moving away from the Clifford limit by introducing infinitesimal coherent noise, an RG flow sets in and percolation flows to Nishimori criticality, making the latter the universal fixed point in the presence of both noise channels. We demonstrate this flow by calculating a number of characteristic properties of the critical theories along the threshold line, including central charge estimates, critical exponents, along with various cumulants.

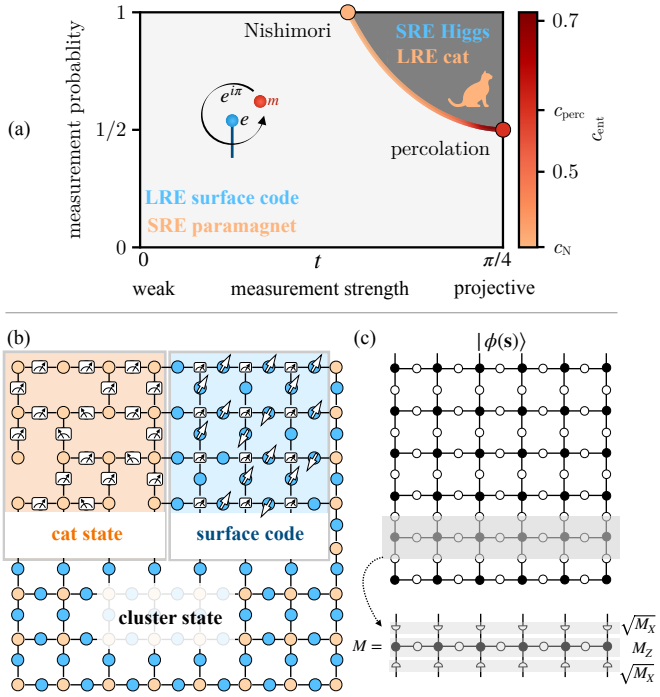

FIG. 1. **Entanglement phase diagram, protocols and tensor network**. (a) Long-range entanglement phase diagram of GHZ-class cat state *or* topological surface code, driven by random and weak measurements. (b) Protocol starting from a parent cluster state. Projectively measuring out the bond qubits results in tunably weak parity measurement: $\exp(-\beta s_{ij} Z_i Z_j/2)$ for the adjacent sites, that leads to a cat state for the site qubits [26]. Projectively measuring out the site qubits results in a surface code for the bond qubits, which can be further subject to weak measurements $\exp(\beta s_{ij} Z_{ij}/2)$ with a probability [2], denoted by the white hollow arrow in the top right "surface code" lattice of panel (b). (c) Tensor network, sliced into a sequence of transfer matrix product operators. Each circle on the bond denotes a matrix, which is chosen to capture the Ising interaction or null interaction depending on the weak or null measurement. Smooth boundary condition is shown, but rough boundary condition for surface code can be implemented by sending the left and right boundary white circles to be identity matrices.

Quantum circuit

Our principal circuit, illustrated in Fig. 1(b), is a shallow (constant-depth) circuit that performs random, weak measurements of either the bond or site qubits on a two-dimensional Lieb lattice. For bond qubit measurements, we start from a product of the Pauli X eigenstate $|+\rangle$ of all N qubits on the sites of the 2D Lieb lattice, for which the protocol then implements ZZ parity check measurements (of tunable strength) resulting in GHZ-class cat states [29]. For site qubit measurements, we start from a pristine toric code state $|\psi_{\rm TC}\rangle$, for which the protocol then implements Z measurements (of tunable strength). These two processes are *dual* [30] to one another which can be seen, for instance, when inspecting their respective wave functions in a representation as (random) 2D projected entangled pair states of the form

$$
\begin{aligned}
|\psi(\mathbf{s})\rangle_{\rm cat} &\propto \exp\left(\frac{\beta}{2}\sum_{ij\in\mathcal{C}} s_{ij} Z_i Z_j\right)|+\rangle \ , \\
|\psi(\mathbf{s})\rangle_{\rm code} &\propto \exp\left(\frac{\beta}{2}\sum_{ij\in\mathcal{C}} s_{ij} Z_{ij}\right)|\psi_{\rm TC}\rangle \ ,
\end{aligned}
\tag{1}
$$

where j denotes sites of the square lattice, Z_{ij} specifies the qubit on the bond center between site i and j, $s_{ij} = \pm 1$ is the measurement outcome on a bond, $\mathbf{s} := \{s_{ij}\}$ denotes the set of all measurement outcomes, and $\mathcal{C}$ denotes the set of bonds that are measured. Wegner's duality maps the domain wall degree of freedom $Z_i Z_j = \pm 1$ on a bond $\langle ij\rangle$ to a spin residing on the bond center $Z_{ij} = \pm 1$. Thus the paragmagnet $|+\rangle$ with proliferated domain walls is mapped to the toric code state $|\psi_{\rm TC}\rangle$ as a loop condensate [31]. Each weak measurement is achieved by projectively measuring an auxilliary qubit that is entangled with the desired observable [26]. The measurement strength $\beta \in [0, +\infty)$ can be tuned by a gate parameter $t \in [0, \pi/4]$ for the entangling gate between each system qubit and the auxiliary qubit through $\tanh(\beta) = \sin(2t)$ [26]. N is the total number of sites, and $N_M = N_B \cdot p_{\rm meas}$ is the total number of measured bonds that are chosen randomly with measurement probability $p_{\rm meas}$. $|\psi_{\rm TC}\rangle$ is the perfect surface code state, dual to the paramagnet state $|+\rangle^{\otimes N}$. $|\psi(\mathbf{s})\rangle_{\rm cat}$ are cat states prepared by *weak* parity measurements [26] over randomly chosen bonds of a square lattice, where the nonuniform measurement can be attributed to the loss of ancilla qubits. $|\psi(\mathbf{s})\rangle_{\rm code}$ are surface code states subject to *weak measurements* for randomly chosen physical qubits [2]. The finite probability of weak measurements can arise from the auxiliary qubit loss or erasure errors.

The two protocols remain *dual* to each other in the presence of errors and share the same phase transition. To see this, let us expand the 2D wave function (1) in the computation basis: $\sum_\sigma \exp\left(\beta/2 \sum_{\langle ij\rangle\in\mathcal{C}} s_{ij}\sigma_i\sigma_j\right)\cdot|\{\sigma_i\}\rangle$, where the wave function amplitude can be interpreted as square root of Bolztmann weight of a classical statistical model, akin to a

Rokhsar-Kivelson (RK) type of state [32–34]. Consequently, Born's rule for measurement outcomes allows us to interpret the probability distribution function of the state in one-to-one correspondence to the partition function of the classical statistical model,

$$P(\mathbf{s}) = \langle\psi(\mathbf{s})|\psi(\mathbf{s})\rangle \propto \sum_{\sigma} \exp\left(\beta \sum_{\langle ij\rangle\in\mathcal{C}} s_{ij}\sigma_i\sigma_j\right), \quad (2)$$

where $\mathcal{C}$ denotes the set of measured bonds, i.e. the geometric connected [35] cluster on which the effective statistical model is supported – this is an incarnation of the random bond Ising model (RBIM) with random bond dilution (see, e.g., Ref. 36). For $p_{\text{meas}} = 1$ (i.e. when all bonds are being subject to measurements) this model reduces to the standard RBIM on a square lattice [26, 37], with $P(\mathbf{s})$ capturing the partition function in the presence of disorder realizations $\mathbf{s}$ whose characteristics are tuned by the measurement strength $0 \le t \le \pi/4$, with a Nishimori transition occurring at intermediate strength $t_c \approx 0.143\pi$. In the projective measurement limit $t = \pi/4$, where the circuit falls into the Clifford class [4, 19, 20, 38], we can sweep $0 \le p_{\text{meas}} \le 1$ to deplete the number of measured bonds, which induces a percolation transition at $p_{\text{meas}} = 1/2$ on the square lattice. Beyond these two limits, we obtain the numerically computed global phase diagram for arbitrary combinations (t, p_{meas}) of measurement strength and bond dilution as shown in Fig. 1(a). Our focus will be on the critical line connecting the two critical points introduced above.

Equivalent (1+1)D monitored circuit dynamics

One useful alternative perspective is to view the 2D quantum problem as a (1+1)D quantum problem using the transfer matrix. The transfer matrix for the evolution at a given time slice t can be decomposed as $M(t) = \sqrt{M_X}\cdot M_Z(t)\cdot\sqrt{M_X}$, where $M_Z(t)$ and M_X are the Ising interaction evolution and transverse field evolution gates

$$M_Z(y) = \exp\left(\beta \sum_{x=1}^{L_x} s_x(y) Z_x Z_{x+1}\right), \; M_X = \exp\left(\beta' \sum_{x=1}^{L_x} X_x\right), \quad (3)$$

where $s_x(y) = \pm 1$ is the bond disorder at site x and time y, after a gauge transformation that fixes the coupling sign of the temporal links, see Appendix A 1. $\beta' = -\frac{1}{2}\ln\tanh(\beta)$ is the Kramers-Wannier dual of β. This (1+1)D quantum model is an *imaginary-time evolving kicked Ising chain* with bond randomness in the Ising interaction that fluctuates in space and time. The probability $P(\mathbf{s})$, Eq. (2), which equals the partition function of the classical 2D Ising model, reading

$$P(\mathbf{s}) = \langle +|\phi(\mathbf{s})\rangle, \text{ where } |\phi(\mathbf{s})\rangle := \prod_{y=1}^{L_y} M(y)\,|+\rangle, \quad (4)$$

(assuming the same boundary conditions at $y = 1$ and $y = L_y$ in Eq. (2), which were left unspecified in the latter equation). Since the physical qubits of the 2D bulk are traced out, such a 1D quantum state $|\phi(\mathbf{s})\rangle$ describes the complexity of the 2D bulk [39], and is related to the diagonal elements of the (mixed state) boundary density matrix [40]. In the Clifford limit $t = \pi/4$ (projective measurement [38]), the effective (1+1)D circuit with random bond dilution is equivalent to the projective measurement-only Ising model, whose phase transition has been demonstrated to fall into the percolation universality class [18–20]. In the non-diluted limit $p_{\text{meas}} = 1$, the resulting (1+1)D circuit is a 1D deep measurement-only quantum circuit representation of the 2D RBIM (which was discussed in the statistically space-time dual version of the same transfer matrix description as above in Ref. [41]), which undergoes a Nishimori transition at $t_c \approx 0.143\pi$ (along the Nishimori line).

Our model thus generalizes the projective Ising model to weak measurements and beyond the Clifford regime. We will show in the following that the percolation criticality of the Clifford limit is a singular point and will be immediately overwritten by the Nishimori universality class upon introducing non-Clifford elements.

Numerical simulations

At the core our our numerical approaches, we generate a set of measurement outcomes $\mathbf{s}$ by uncorrelated sampling followed by gauge symmetrization, as described in Ref. [26]. Compared with the relatively modest sizes $L \sim \mathcal{O}(10)$ of Ref. [26], here we can collect data of much bigger system sizes $L \sim \mathcal{O}(10^3)$ because the whole phase diagram of interest has a *gauge symmetry* (see Appendix) that allows us to simplify the sampling of the measurement outcomes by means of gauge fixing. Using these sampled configurations, we employ three numerical methods to analyze the entanglement properties and phase transitions in our model.

The most versatile of these is the *tensor network* contraction method, which enables us to compute the coherent information I_c and the entanglement entropy S across the full phase diagram. This approach allows us to access system sizes up to $(L+1)\times L$ with linear system sizes as large as $L = 512$ for I_c, and up to $L\times 2L$ with $L = 1024$ for S on long stripe geometries (open boundary conditions). For each fixed disorder realization, the qubit-based tensor network can be fermionized into a Gaussian fermion tensor network akin to the Chalker-Coddington network model [24, 40, 42] which allows efficient contraction in periodic boundary conditions without truncation, which we use for the multifractality calculations below.

To target specific critical points in periodic boundary conditions, we also utilize *Clifford circuit* simulations at the percolation point and a *Majorana fermion evolution* technique at the Nishimori point. Both methods are used to compute S on long cylinder geometries: $L\times 4L$ with $L = 1024$ for the Clifford simulations, and $L\times 20L$ with $L = 1024$ for the Majorana approach. In both cases, the system is thermalized for $4L$ time steps prior to calculating the entanglement. For the Majorana simulations, we compute S every $L/2$ time steps after thermalization, reducing computational cost while ensuring sufficient decorrelation between samples.

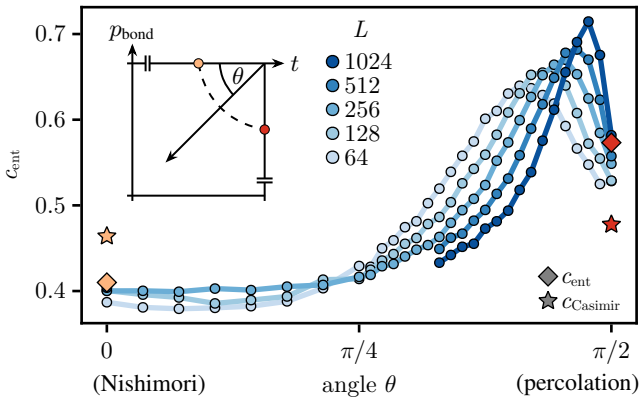

FIG. 2. **Effective central charge on the critical line.** Inset: The angle θ describes the position on the critical line. The Nishimori point corresponds to $\theta = 0$, whereas the percolation point corresponds to $\theta = \pi/2$. The effective central charge governing the average entanglement entropy at Nishimori criticality is numerically computed to be $c_{\rm ent} = 0.41956(3)$ (orange diamond), see Fig. 4. For reference we also show the effective central charge determined by the Casimir energy at the Nishimori point $c_{\rm Casimir} = 0.464(4)$ [43] (orange star). At the percolation critical point, our numerically determined effective central charge agrees with the analytically known $c_{\rm ent} = \frac{3\sqrt{3}\ln(2)}{2\pi} = 0.573\ldots$ [19] (red diamond), distinct from the Casimir energy estimate $c_{\rm Casimir} = \frac{5\sqrt{3}}{4\pi}\ln 2 = 0.478\ldots$ (red star).

Entanglement entropy of 1D quantum state

In discussing the global phase diagram of Fig. 1(a) our interest lies on the critical theories describing the transition along the line of thresholds, connecting the Nishimori point in the limit of $p_{\rm meas} = 1$ where all bonds are being subject to measurements, and the percolation transition corresponding to the Clifford limit of projective (i.e. "strong") measurements $t = \pi/4$. Since both critical points, the Nishimori point at $p_{\rm meas} = 1$ and the percolation point at $p_{\rm meas} = 1/2$ are monitored quantum systems known to be described by corresponding non-unitary CFTs, we now discuss two universal characteristics of the corresponding non-unitary, logarithmic CFTs [11–15, 40, 44, 45]. These are (i): the so-called "effective central charge", which is a universal critical finite-size scaling amplitude quantifying the Casimir effect of the monitored (i.e. random) CFT, which we here denote by $c_{\rm Casimir}$, and (ii): the universal coefficient of the logarithm of subsystem size of the von Neumann entanglement entropy, which is (twice) the (typical) scaling dimension of a so-called boundary condition changing "twist operator", one located at each end of the entanglement interval [22, 46–48], which we parametrize here by $c_{\rm ent}$. In a monitored (and, more generally, any random) system, the two universal characteristics are in general not equal to each other, i.e. $c_{\rm Casimir} \neq c_{\rm ent}$. Often, both are *incorrectly* referred to as "effective central charge", which easily leads to conceptual confusion. Such confusion originates from the fact that for ground states of a completely standard, non-random, i.e. entirely uniform and translationally invariant unitary CFT, these two universal characteristics coincide, and are equal to the central charge of the unitary CFT. However, in the case of monitoring, or for that matter any source of randomesss which by definition breaks translational invariance, the central charge of the non-unitary CFT simply vanishes [49], and thus carries no information whatsoever which would be capable of distinguishing different critical points. The universal (non-equal) quantities $c_{\rm Casimir}$ and $c_{\rm ent}$, on the other hand, are in general non-vanishing in those latter cases, and are powerful universal charactistics distinguishing *different* monitored (or, in general, random) non-unitary CFTs.

Let us start our discussion with the quantity $c_{\rm ent}$: First let us briefly review the case of the ground state of a standard, translationally invariant CFT. In our model, such a unitary CFT description is relevant to a post-selection scenario with uniform $(s = +1)$ which realizes a disorder-free (1+1)D critical Ising chain with central charge $1/2$ in lieu of the Nishimori critical point upon tuning the measurement strength in the limit of $p_{\rm meas} = 1$. In this case the von Neumann entanglement entropy is well known [50, 51] to take the form (assuming periodic boundary conditions)

$$S_{vN} = \frac{c}{3}\ln\left[\frac{L}{\pi}\sin\left(\frac{\pi l}{L}\right)\right], \tag{5}$$

where $c = 1/2$ for the post-selected Ising case above. A similar expression holds in the case of open boundary conditions where the entanglement interval of size ℓ sits at the boundary of the system, with a prefactor of the logarithm equal to $c/6$ instead of $c/3$. This expression relies solely on the fact that the entanglement entropy is related to the logarithm of the two-point function of the twist-operator, which decays as a power of the chord distance $R = \left[\frac{L}{\pi}\sin\left(\frac{\pi l}{L}\right)\right]$, indicated in Eq. (5), due to periodic boundary conditions in spatial size L. Now moving on to the case of monitoring of interest to us, the expression for the Born-rule averaged entanglement entropy is of the same form

$$\sum_{\mathbf{s}} P(\mathbf{s}) S_{vN}(|\phi(\mathbf{s})\rangle) = \frac{c_{\rm ent}}{3}\ln R\,, \tag{6}$$

where the 1D quantum state $|\phi(\mathbf{s})\rangle$ was defined in Eq. (4). The reason for this form is that again, the entropy is given by the logarithm of the two-point function of the twist operator, but now that twist operator correlation function is random as it depends on the quantum trajectory (it is thus a more complex object), and has to be averaged with the Born rule probability $P(\mathbf{s})$. The result turns out [52] to be the right hand side of Eq. (6). Here the coefficient $c_{\rm ent}$ determines the *average* entanglement entropy of the ensemble of *1D quantum states*. That is, for the Born average scenario, we compute the entanglement entropy for each set of measurement outcomes $\mathbf{s}$ yielding $S_{vN}(|\phi(\mathbf{s})\rangle)$, and average it according to the Born probability.

Let us now turn to a discussion of $c_{\rm Casmir}$. For disordered systems, a quantity directly related to the central charge, called the *effective central charge*, is instead given by the universal prefactor governing the Casimir energy [53–55]. Note that here, the Casimir energy is random depending on the

quantum trajectory. The correct quantity to consider turns out to be the *averaged* Casimir energy, related to the fact that this is a self-averaging quantity. In the language of replicas, the effective central charge is given by the derivative of the central charge of the replicated theory with respect to the number of replicas in the replica limit (which precisely describes [53] the *average* of the Casimir energy in the language of replicas): although the central charge becomes zero in the replica limit, its first derivative is in general non-zero [it is also universal since the central charge is universal for any (sufficiently small) number of replicas]. For instance, in the case of percolation, the following analytical results are known,

$$c_{\text{ent}} = \frac{3\sqrt{3}}{2\pi}\ln 2 = 0.573, \quad c_{\text{Casimir}} = \frac{5\sqrt{3}}{4\pi}\ln 2 = 0.478\,, \tag{7}$$

with c_{ent} first derived in Ref. [56] (see also Ref. 19 and 20 for a later discussion), while c_{Casimir} has been listed in Refs. 20, 36, and 54. Similarly, for the Nishimori critical point (in the absence of bond dilution), those two universal numbers have been obtained numerically to be

$$c_{\text{ent}} = 0.41956(3)\,, \qquad c_{\text{Casimir}} = 0.464(4)\,, \tag{8}$$

where the Casimir estimate, c_{Casimir}, was obtained in classical Monte Carlo simulations via scaling of the free energy of the classical statistical mechanics model formulation in Ref. 43. Our high-precision numerical estimate of c_{ent} reported in the paper at hand is roughly consistent with the one previously obtained by TEBD calculation (albeit only for system sizes up to $L \sim 300$) in Ref. [57].

Looking at the four estimates above, it is clear that they describe two distinct universality classes. But while the Casimir central charge estimates c_{Casimir} for the two critical theories differ only by a few percent, there is a substantial (some 40%) difference for the entanglement entropy prefactor c_{ent} between the two universality classes, making the latter the go-to discriminator between the two theories.

RG flow along the critical line

Let us now shift our attention towards the critical line connecting the percolation and Nishimori critical points in our phase diagram in Fig. 1(a). Along this line we have numerically calculated c_{ent} as shown in Fig. 2 for systems of varying size with up to $N = 1024 \times 2048$ qubits. What we qualitatively find is that upon moving away from the Nishimori critical point upon introducing dilute measurements, our numerical c_{ent} estimate remains constant at first, indicating that the critical theory remains within the Nishimori universality class. But upon approaching the percolation point, a dramatic shift sets in with c_{ent} strongly increasing, overshooting the percolation estimate, which is ultimately approached as one nears the Clifford limit of projective measurements. This non-monotonous behavior of c_{ent} along the critical line of non-unitary theories should be contrasted to the strict monotonicity dictated by the c-theorem for uniform, translationally invariant unitary CFTs [58], but which generally not apply to the non-unitary case. Indeed, it has been shown that entanglement does not decrease monotonically under renormalization flows for certain models, see *e.g.* [59, 60]. One way to rationalize this non-monotonous behavior in our model is to realize that when moving away from the percolation transition, our system leaves the constrained Hilbert space available to the Clifford circuit which allows the wavefunction to suddenly populate an extensive number of states in the full Hilbert space – a situation that might well lead to a sharp increase in the entanglement and therefore a larger c_{ent} estimate.

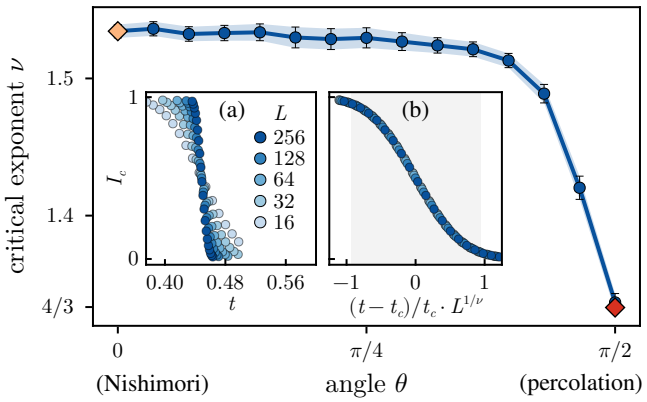

FIG. 3. **Critical exponent ν on the critical line.** We calculate the critical exponent ν for different angles θ on the critical line by finite-size scaling for the coherent information of the surface code (with code distance $L = L_x - 1 = L_y$ up to $L = 512$ on the Nishimori line and up to $L = 256$ elsewhere). At the Nishimori point we obtain a value of $\nu = 1.532(4)$ (orange diamond). At the percolation point we determine $\nu = 1.337(6)$, which is consistent with the analytical value [61] $\nu = 4/3$ (red diamond). Inset (a) shows the raw data for different system sizes and inset (b) shows their data collapse for the Nishimori point ($\theta = 0$).

Beyond the non-monotonicity, the qualitative behavior of c_{ent} along the critical line allows for the identification of a renormalization group (RG) flow of the critical theory. With all the action taking place in proximity of the percolation transition, this is where the RG flow happens – that is, upon moving away from the percolation critical point the system flows to Nishimori universality. This direction of the flow can be established analytically by demonstrating the irrelevance of random bond dilution at the Nishimori critical point, using the known numerical results for the correlation length exponents (and a Harris-criterion type argument): Dilution couples to the thermal/energy operators at the Nishimori point, which have scaling dimensions [62] $x_1 = 1.345$ and $x_2 = 1.75$ respectively. The scaling dimension of the operator coupling to the strength of dilution is twice as large deduced from the replica trick, i.e. $x_{\text{dilution}} = 2.69$, which is larger than 2 and thus irrelevant (for the two dimensional scenario we are looking at). This is the "Harris-type criterion" [63, 64] stating irrelevance if the dimension of the energy operator is larger than one (or the correlation length exponent associated with it $\nu > 1$) – in two dimensions. We also note that previous high-precision calculations on the classical diluted RBIM [36] have studied

the behavior of the c_{Casimir} and through very careful simulations (tuning three parameters in the classical model instead of two parameters in our quantum model) have similarly concluded that percolation must be unstable to a flow to Nishimori criticality.

Moving away from the entanglement diagnostic, let us also analyze the correlation length exponent ν which corroborates the RG flow as shown in Fig. 3. We compute this exponent via a coherent information estimate in the surface code protocol [2], an observable that shows a finite-size independent crossing point (i.e. a zero scaling dimension) at the transition and whose data collapse therefore allows for high-precision estimates of the correlation length exponent.

Multifractality

To further analyze the universal properties of the percolation and Nishimori critical points, we study their "multifractal" spectra of scaling dimensions. Since measurement outcomes are random, the monitored systems studied in this paper are intrinsically *disordered*. The corresponding critical points and conformal field theories are much richer than their clean, unitary counterparts, as one can distinguish, for example, mean and typical correlation functions. More generally, different moments of correlations functions scale with distinct non-trivial exponents [65], a phenomenon known as multifractality (sometimes also referred to as 'multiscaling') in the literature of disordered critical points. This leads to a *continuous* spectrum of universal critical exponents (scaling dimensions). We will focus on the scaling behavior of the boundary condition changing (boundary) twist operators [21, 47] whose typical scaling dimensions give rise to the universal prefactors in the Rényi entropies, which we referred to as c_{ent} for the von Neumann entropy and which we denote by $c_{\text{ent}}^{(n)}$ for the nth Rényi entropy. The multifractal scaling behavior quantifies the universal scaling behavior of the *statistical fluctuations* of these entropies. There is an infinite set of universal quantities for each of the nth Rényi entropies characterizing these fluctuations. Here we follow the discussion in Ref. [23] where this is spelled out in detail for the $n = 2$nd Rényi entropy (the discussion being analogous for general n), see Appendix A 4 for a self-contained summary. In the following we discuss and numerically compute these statistical fluctuations for the von Neumann entropy. In the previous section we have discussed the Born average of the boundary von Neumann entanglement entropies, which reveals only the first moment of the random variable $\{S_{vN}(\mathbf{s})\}$ (here we abbreviate $|\phi(\mathbf{s})\rangle$ by $|\phi\rangle$ inside the argument). It turns out that higher cumulants (with κ_m denoting the m^{th} cumulant) of this quantity also scale logarithmically at criticality, with universal prefactors,

$$\begin{aligned}\kappa_2 &= \mu_2 - \mu_1^2 = -2x^{(2)} \ln R\,,\\ \kappa_3 &= \mu_3 - 3\mu_2\mu_1 + 2\mu_1^3 = 2x^{(3)} \ln R\,,\end{aligned} \tag{9}$$

and more generally

$$\kappa_m = (-1)^{m-1} 2x^{(m)} \ln R\,, \tag{10}$$

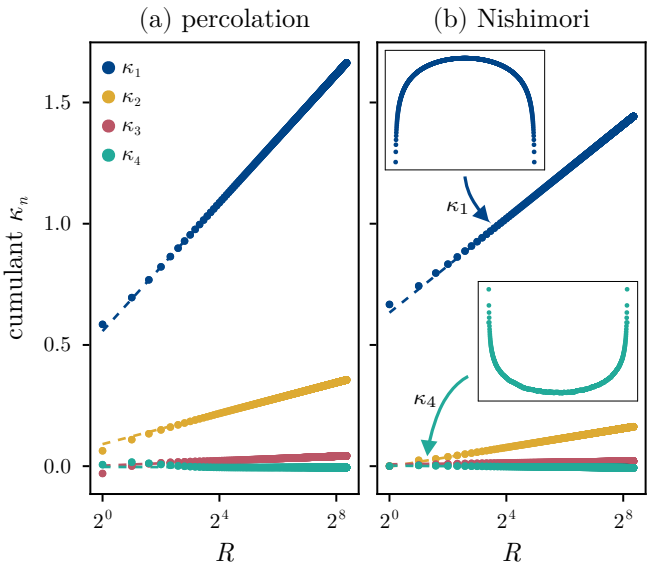

FIG. 4. **Multifractality** of percolation and Nishimori criticality. Shown are the first four cumulants, $\kappa_1, \kappa_2, \kappa_3$ and κ_4 of the von Neumann entropy as a function of chord distance. Note that the fourth-order cumulant κ_4 shows a sign-flip with an inverted 'entanglement arc' [cf. Eq. (5)] as shown in the inset.

with $\mu_m = \sum_{\mathbf{s}} P(\mathbf{s})[S_{vN}(\mathbf{s})]^m$ being the m-th moment average and R the chord length. Here $x^{(m)}$ adopts the notation from Ref. [23], which expresses the scaling of the cumulants of the entanglment entropy (a random variable) with $\ln R$, for different cumulant orders m, and $x^{(1)} = c_{\text{ent}}/6$ in our notation.

As already mentioned above, different from Ref. [23] here we mainly consider the von Neumann entropy in the main text, while leaving a discussion of the higher-order Rényi entropies for the Appendix. In Fig. 4, we show the scaling of the cumulants with chord length which yields a spectrum of universal numbers $x^{(m)}$ that are distinct between Nishimori and percolation criticality as summarized in Table I. Remarkably, contrary to what was previously assumed, even percolation exhibits a non-trivial multifractal spectrum with non-trivial values for the set of universal numbers $x^{(m)}$. The multifractal behavior of entanglement in the percolation theory can be understood as follows: entanglement in this theory is related to the number of percolation clusters connecting the entanglement interval to its complement. This quantity has a non-trivial statistics, which was computed exactly in Ref. [56] using Coulomb gas methods. The results can be conveniently expressed in terms of the k-th moment average of the n-th order generalized purity (defined in Eq. (11) below, the standard purity corresponding to $n = 2$) in the Born ensemble

$$\overline{[\text{tr}(\rho(\mathbf{s}))^n]^k} = \overline{e^{-k(n-1)S_n(\mathbf{s})}} \propto R^{-2X_{n,k}}\,, \tag{11}$$

where the overbar denotes the average with respect to the Born rule probability distribution for the measurement outcomes "$(\mathbf{s})$". Eq. (11) describes the k-th moment of a boundary two-point function of boundary-condition changing (bcc) "twist"

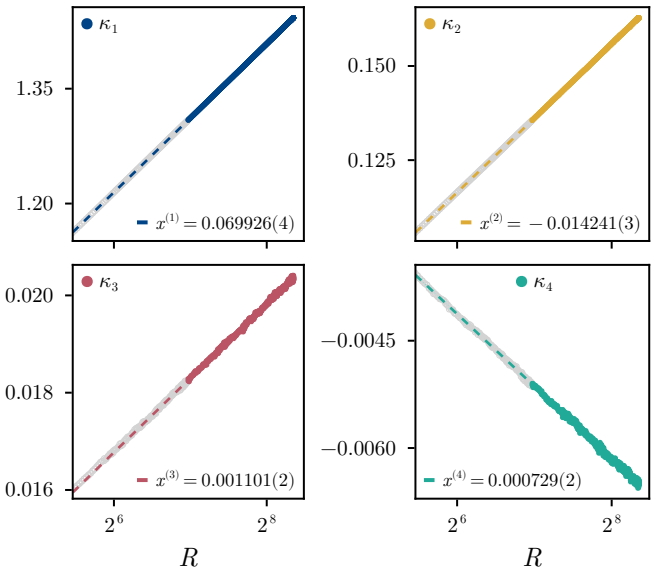

FIG. 5. **Cumulant fits for Nishimori universality.** Shown is a subset of the data of Fig. 4(b), with the color-highlighted data used in the fits indicated by the dashed lines over the remaining data (gray). The data is fitted using Eq. (9) to obtain the numerical estimates indicated in the figure (and listed in Table I) To minimize boundary effects we fit only the data in an intermediate window of large cut length $L_x/8 < l < 7L_x/8$, see Appendix B 3 for supplemental data and a detailed discussion.

operators [21, 23, 47] separated by the chord-length R. For percolation (which can be formulated as a particular Clifford circuit [18–20]), this quantity does not depend on the Rényi index n, and the scaling dimension $X_{n,k} = X_k$ is the generating function $X_k = \sum_m \frac{x^{(m)}}{m!} k^m$ of the universal coefficients appearing in Eq. (9) [23]. In this case we may choose $n = 2$, and Eq. (11) describes the k-th moment of the (standard) purity. Using the results of Ref. [56], we find that for percolation, we have the exact multifractal spectrum of critical exponents

$$X_k = \frac{3\arccos^2(\sqrt{3}/2^{1+k/2})}{2\pi^2} - \frac{1}{24}\,. \tag{12}$$

with

$$\begin{aligned} x^{(1)} &= c_{\text{ent}}/6 = \frac{\sqrt{3}}{4\pi}\ln 2 \simeq 0.09554\,,\\ x^{(2)} &= -0.022914\,,\\ x^{(3)} &= 0.0034922\,,\\ x^{(4)} &= 0.0002325\,,\\ x^{(5)} &= -0.0002561\,. \end{aligned} \tag{13}$$

Note that with our conventions [Eq. (10)], $x^{(2)}$ is negative by definition since the variance must be positive. Further note that the positiveness of $x^{(4)}$ predicts that the 4th cumulant $\kappa_4 = -2x^{(4)} \ln R$ scales, following Eq. (5), as an inverted 'entanglement arc' (see the inset of Fig. 4 for an example). Extracting numerically the asymptotic behavior of higher cumulants is extremely challenging as it requires multiple cancellations between powers $(\ln R)^k$ where the chord length R is large in the limit of interest in Eq. (9), and we need to extract the coefficient of the lowest, first-order power of this large quantity $\ln R$ [see Eq. (9)]. Nevertheless, we find that for our numerical results for critical percolation [Fig. 4(a)] the first two significant digits generally agree well with the exact results, see also the side-by-side comparison of Table I above. For the percolation problem, fitting the fourth-order cumulant remains a difficult endeavor and, to some extent, we have 'cherry-picked' the fitting range to match the analytical expectation (see Fig. 10 in the Appendix for further details).

Surprisingly, it turns out that the numerical estimates for Nishimori criticality, shown in Fig. 4(b) and also summarized in Table I, converge significantly faster – intuitively, this makes sense since the Clifford/percolation data involves averaging *discrete* quantities, and thus requires more samples. Our analysis of the von Neumann entropy yields the following values

$$\begin{aligned} x^{(1)} &= 0.069926(4)\,,\\ x^{(2)} &= -0.014241(3)\,,\\ x^{(3)} &= 0.001101(2)\,,\\ x^{(4)} &= 0.000729(2)\,, \end{aligned} \tag{14}$$

which are also listed in Table I in the column denoted von Neumann and compared to results from the second, third, and $n = \infty$ Rényi entropies as indicated in the column headers.

To summarize these results, it is quite notable that the two monitored (non-unitary) critical points studied here, percolation and Nishimori criticality, both contain an *infinite* set of scaling dimensions that constitute a *continuous* spectrum in contrast to conventional (unitary) critical points. This richness of critical exponents originates from the random nature of monitored criticality and reflects their multifractality. For percolation, we have been able to compute the entire (non-quadratic) multifractal spectrum exactly, while for Nishimori criticality our numerical simulations allowed to access the leading five cumulants.

Discussion

It is conceptually important to note the following two equivalent roles that percolation plays in our work: While we have so-far employed percolation as a means to simply describe the *geometrically* and purely classical random dilution of bonds of the 2D lattice on which the RBIM quantum mechanics (viewed as a shallow quantum circuit on a 2D spatial lattice, in an Rokhsar-Kivelson (RK) formulation as mentioned above) is located, percolation itself can be viewed as a deep (1+1)D random Clifford circuit of projective measurements on the 1D lattice [18–20, 66, 67] whose spacetime is the above 2D lattice. The 2D quantum states on the critical, geometric percolation cluster, i.e. at $p_{meas} = 1/2$ and $t = \pi/4$ in our phase diagram in Fig. 1, can be exactly mapped to such a deep (1+1)D Clifford circuit with random projective measurements, which represents the geometrical percolation problem in spacetime

criticality	**percolation**		**Nishimori**			
ν	4/3		1.532(4)			
$c_{\rm ent}^{\rm vN}$	$0.573\ldots$		0.41956(3)			
$c_{\rm Casimir}$	$0.478\ldots$		0.464(4)			
cumulants	analytical	numerical	von Neumann	Rényi-2	Rényi-3	Rényi-∞
$x^{(1)}$	0.09554	0.09556(1)	0.069926(4)	0.054841(4)	0.049519(3)	0.038573(3)
$x^{(2)}$	−0.02291	−0.02289(1)	−0.014241(3)	−0.012317(2)	−0.011287(2)	−0.007834(1)
$x^{(3)}$	0.00349	0.00348(1)	0.001101(2))	0.001433(2)	0.001517(1)	0.001231(1)
$x^{(4)}$	0.00023	0.00021(2)*	0.000729(2)	0.000644(1)	0.000557(1)	0.000200(1)
$x^{(5)}$	−0.00026	—	0.000050(2)†	−0.000128(1)	−0.000209(1)	−0.000189(1)

TABLE I. **Characterization of critical points.** For percolation, we list analytical results for the critical exponents, effective and entanglement central charge estimates, along with the five leading cumulants for the $n = 1$ von Neumann entanglement entropy, as defined in Eq. (10). We also provide numerical estimate for these cumulants, extracted from fits like the ones shown in Fig. 4(a). The asterisk (*) for the fourth-order cumulant indicates that we needed to "cherry-pick" the fitting interval in order to reproduce a value close to the analytical estimate (see Fig. 10 of the Appendix). For Nishimori criticality, no analytical results are known and we list our numerical estimates. Note that for the cumulant estimates we are able to obtain high-precision results for the leading four cumulants from the fits shown in Fig. 5 and even a rough estimate for the fifth-order one (see Fig. 10(b) of the Appendix for the underlying fit). These Nishimori cumulants we have calculated not only from the von Neumann entanglement entropy but also the second, third and $n = \infty$ order Rényi entropies as indicated. The dagger ($\dagger$) for the fifth-order von Neumann cumulant of Nishimori criticality indicates that it is likely unreliable given that there is a "flip" in the entanglement arc that might arise from boundary or finite-size effects, see Fig. 10 in the Appendix.

in a quantum mechanical (1+1)D deep circuit language. The percolation criticality is well known to have a flat entanglement spectrum because it can be thought of as a deep Clifford circuit [18–20] and thus all Rényi entropies are trivially identical in every quantum trajectory. Nevertheless, here we show analytically that the statistical ensemble of the entanglement entropies over different quantum trajectories exhibits *multifractality*, which is further evidenced by our numerical computation of the cumulants of these entanglement entropies up to 3rd, 4th, and 5th cumulants, that are elusive in the literature.

Moving away from the point of percolation criticality ($p_{\rm meas} = 1/2$, $t = \pi/4$) in our phase diagram along the critical RG crossover line, is a concrete way of "turning on" the non-Clifford perturbations at the percolation critical point of the (1+1)D deep Clifford circuits. These arise from the additional quantum mechanics of the Nishimori measurements, which can be induced by weakening the projective measurements [26], or by injecting coherent error prior to measurements [28, 68–70] in the Clifford circuit.

More generally, the measurement-induced phase transitions we reveal here can also be viewed [40] as a mixed state transition for the classical-quantum mixed state $\rho = \sum_{\mathbf{s}} |\mathbf{s}\rangle\langle\mathbf{s}| \otimes |\psi(\mathbf{s})\rangle\langle\psi(\mathbf{s})|$, where $|\mathbf{s}\rangle\langle\mathbf{s}|$ denotes the state of ancilla qubits that record the measurement outcomes, and we take $|\psi(\mathbf{s})\rangle$ to be the toric code state subjected to diluted weak measurements, as written in Eq. (1). It can be shown that the *same* universality class describes the mixed state subjected to a diluted dephasing noise channel instead of quantum measurement, see Fig. 6 for a schematic and Appendix A for details. Here we outline the basic idea as follows: When the measurement outcomes are erased (i.e. traced over), the observer acts as a bath, and the ensemble of the post-measurement states is no longer an ensemble of pure states, but simply gives rise to a mixed state. Effectively, the toric code is subjected to a diluted dephasing channel [2] with noise probability $\sin^2(t)$; see Appendix A for a detailed discussion. In the non-dilute limit $p_{meas} = 1$ with uniform dephasing noise (top line of our phase diagram Fig. 1), the noisy toric code exhibits a Nishimori transition [1], albeit at a smaller threshold $t_c \approx 0.107\pi$ [2] – see the schematic illustration of Fig. 6. In the maximally noisy limit $t = \pi/4$ with noise hitting only a fraction of the qubits, the state again undergoes the same percolation transition at $p_{meas} = 1/2$. Thus, for the noisy state after erasure (tracing out) of the measurement record $\mathbf{s}$, the phase boundary between toric code and dephased toric code extends from the same percolation critical point to a Nishimori critical point (at $t_c \approx 0.107\pi$), which is described by the same RG flow as revealed in this manuscript.

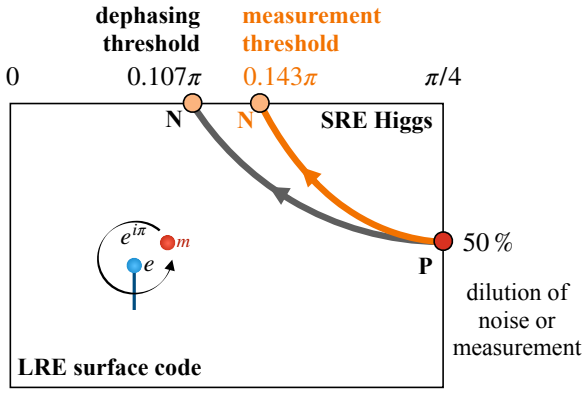

FIG. 6. **Schematic phase diagram of diluted noise channel in comparison with diluted measurement** of the topological toric code or surface code. Both exhibit a critical line from percolation to the Nishimori points, albeit at different threshold values.

Data availability.– The numerical data shown in the figures and the data for sweeping the phase diagram is available on Zenodo [71].

ACKNOWLEDGMENTS

The Cologne group gratefully acknowledge partial funding from the Deutsche Forschungsgemeinschaft (DFG, German Research Foundation) under Germany's Excellence Strategy – Cluster of Excellence Matter and Light for Quantum Computing (ML4Q) EXC 2004/1 – 390534769 and within the CRC network TR 183 (Project Grant No. 277101999) as part of subproject B01. R.V. acknowledges partial support from the US Department of Energy, Office of Science, Basic Energy Sciences, under award No. DE-SC0023999. G.-Y. Z. acknowledges support from the Faculty Startup Fund at the Hong Kong University of Science and Technology (Guangzhou). The numerical simulations were performed on the JUWELS cluster at the Forschungszentrum Juelich.

[1] E. Dennis, A. Kitaev, A. Landahl, and J. Preskill, Topological quantum memory, Journal of Mathematical Physics **43**, 4452 (2002).
[2] F. Eckstein, B. Han, S. Trebst, and G.-Y. Zhu, Robust Teleportation of a Surface Code and Cascade of Topological Quantum Phase Transitions, PRX Quantum **5**, 040313 (2024).
[3] M. Grassl, T. Beth, and T. Pellizzari, Codes for the quantum erasure channel, Phys. Rev. A **56**, 33 (1997).
[4] T. M. Stace, S. D. Barrett, and A. C. Doherty, Thresholds for Topological Codes in the Presence of Loss, Phys. Rev. Lett. **102**, 200501 (2009).
[5] P. Scholl, A. L. Shaw, R. B.-S. Tsai, R. Finkelstein, J. Choi, and M. Endres, Erasure conversion in a high-fidelity Rydberg quantum simulator, Nature **622**, 273 (2023).
[6] J. D. Teoh, P. Winkel, H. K. Babla, B. J. Chapman, J. Claes, S. J. de Graaf, J. W. O. Garmon, W. D. Kalfus, Y. Lu, A. Maiti, K. Sahay, N. Thakur, T. Tsunoda, S. H. Xue, L. Frunzio, S. M. Girvin, S. Puri, and R. J. Schoelkopf, Dual-rail encoding with superconducting cavities, Proceedings of the National Academy of Sciences **120**, e2221736120 (2023).
[7] D. E. Browne, M. B. Elliott, S. T. Flammia, S. T. Merkel, A. Miyake, and A. J. Short, Phase transition of computational power in the resource states for one-way quantum computation, New Journal of Physics **10**, 023010 (2008).
[8] M. Pant, D. Towsley, D. Englund, and S. Guha, Percolation thresholds for photonic quantum computing, Nature Communications **10**, 1070 (2019).
[9] S. Chirame, A. Prem, S. Gopalakrishnan, and F. J. Burnell, Stabilizing Non-Abelian Topological Order against Heralded Noise via Local Lindbladian Dynamics, arXiv 2410.21402.
[10] D. Stauffer and A. Aharony, (Taylor & Francis, 1992).
[11] V. Gurarie, Logarithmic operators in conformal field theory, Nuclear Physics B **410**, 535 (1993).
[12] V. Gurarie and A. W. W. Ludwig, Conformal field theory at central charge c=0 and two-dimensional critical systems with quenched disorder, in From Fields to Strings: Circumnavigating Theoretical Physics (World Scientific, 2005) pp. 1384–1440.
[13] V. Gurarie, c-Theorem for disordered systems, Nuclear Physics B **546**, 765 (1999).
[14] R. Vasseur, J. L. Jacobsen, and H. Saleur, Logarithmic observables in critical percolation, Journal of Statistical Mechanics: Theory and Experiment **2012**, L07001 (2012).
[15] J. Cardy, Logarithmic conformal field theories as limits of ordinary CFTs and some physical applications, Journal of Physics A: Mathematical and Theoretical **46**, 494001 (2013).
[16] M. P. Fisher, V. Khemani, A. Nahum, and S. Vijay, Random Quantum Circuits, Annual Review of Condensed Matter Physics **14**, 335 (2023).
[17] A. C. Potter and R. Vasseur, Entanglement dynamics in hybrid quantum circuits (2021).
[18] A. Nahum and B. Skinner, Entanglement and dynamics of diffusion-annihilation processes with Majorana defects, Phys. Rev. Res. **2**, 023288 (2020).
[19] N. Lang and H. P. Büchler, Entanglement transition in the projective transverse field Ising model, Phys. Rev. B **102**, 094204 (2020).
[20] A. Kumar, K. Aziz, A. Chakraborty, A. W. W. Ludwig, S. Gopalakrishnan, J. H. Pixley, and R. Vasseur, Boundary transfer matrix spectrum of measurement-induced transitions, Phys. Rev. B **109**, 014303 (2024).
[21] C.-M. Jian, Y.-Z. You, R. Vasseur, and A. W. W. Ludwig, Measurement-induced criticality in random quantum circuits, Phys. Rev. B **101**, 104302 (2020).
[22] Y. Bao, S. Choi, and E. Altman, Theory of the phase transition in random unitary circuits with measurements, Phys. Rev. B **101**, 104301 (2020).
[23] Y. Li, R. Vasseur, M. P. A. Fisher, and A. W. W. Ludwig, Statistical mechanics model for Clifford random tensor networks and monitored quantum circuits, Phys. Rev. B **109**, 174307 (2024).
[24] C.-M. Jian, B. Bauer, A. Keselman, and A. W. W. Ludwig, Criticality and entanglement in nonunitary quantum circuits and tensor networks of noninteracting fermions, Phys. Rev. B **106**, 134206 (2022).
[25] D. Gottesman, Stabilizer Codes and Quantum Error Correction (1997), arXiv.quant-phys:9705052.
[26] G.-Y. Zhu, N. Tantivasadakarn, A. Vishwanath, S. Trebst, and R. Verresen, Nishimori's Cat: Stable Long-Range Entanglement from Finite-Depth Unitaries and Weak Measurements, Phys. Rev. Lett. **131**, 200201 (2023).
[27] J. Y. Lee, W. Ji, Z. Bi, and M. P. A. Fisher, Decoding Measurement-Prepared Quantum Phases and Transitions: from Ising model to gauge theory, and beyond, arXiv 2208.11699.
[28] E. H. Chen, G.-Y. Zhu, R. Verresen, A. Seif, E. Bäumer, D. Layden, N. Tantivasadakarn, G. Zhu, S. Sheldon, A. Vishwanath, S. Trebst, and A. Kandala, Nishimori transition across the error threshold for constant-depth quantum circuits, Nature Physics **21**, 161 (2025).
[29] H. J. Briegel and R. Raussendorf, Persistent Entanglement in Arrays of Interacting Particles, Phys. Rev. Lett. **86**, 910 (2001).
[30] F. J. Wegner, Duality in Generalized Ising Models and Phase Transitions without Local Order Parameters, Journal of Mathematical Physics **12**, 2259 (1971).
[31] A. Y. Kitaev, Fault-tolerant quantum computation by anyons , Annals of Physics **303**, 2 (2003).
[32] C. L. Henley, From classical to quantum dynamics at

Rokhsar–Kivelson points, Journal of Physics: Condensed Matter **16**, S891 (2004).
[33] E. Ardonne, P. Fendley, and E. Fradkin, Topological order and conformal quantum critical points, Annals of Physics **310**, 493 (2004).
[34] S. V. Isakov, P. Fendley, A. W. W. Ludwig, S. Trebst, and M. Troyer, Dynamics at and near conformal quantum critical points, Phys. Rev. B **83**, 125114 (2011).
[35] We need to be above the percolation threshold, $p_{meas} \geq 1/2$.
[36] M. Picco, A. Honecker, and P. Pujol, Strong disorder fixed points in the two-dimensional random-bond Ising model, Journal of Statistical Mechanics: Theory and Experiment **2006**, P09006 (2006).
[37] J. Y. Lee, W. Ji, Z. Bi, and M. P. A. Fisher, Measurement-Prepared Quantum Criticality: from Ising model to gauge theory, and beyond, arXiv (2022), 2208.11699.
[38] D. Lee and B. Yoshida, Randomly Monitored Quantum Codes, arXiv 2402.00145.
[39] J. C. Napp, R. L. La Placa, A. M. Dalzell, F. G. S. L. Brandão, and A. W. Harrow, Efficient Classical Simulation of Random Shallow 2D Quantum Circuits, Phys. Rev. X **12**, 021021 (2022).
[40] Q. Wang, R. Vasseur, S. Trebst, A. W. W. Ludwig, and G.-Y. Zhu, Decoherence-induced self-dual criticality in topological states of matter, arXiv e-prints 2502.14034.
[41] I. A. Gruzberg, N. Read, and A. W. W. Ludwig, Random-bond Ising model in two dimensions: The Nishimori line and supersymmetry, Phys. Rev. B **63**, 104422 (2001).
[42] F. Merz and J. T. Chalker, Two-dimensional random-bond Ising model, free fermions, and the network model, Phys. Rev. B **65**, 054425 (2002).
[43] A. Honecker, M. Picco, and P. Pujol, Universality Class of the Nishimori Point in the 2D $\pm J$ Random-Bond Ising Model, Phys. Rev. Lett. **87**, 047201 (2001).
[44] A. Zabalo, M. J. Gullans, J. H. Wilson, R. Vasseur, A. W. W. Ludwig, S. Gopalakrishnan, D. A. Huse, and J. H. Pixley, Operator Scaling Dimensions and Multifractality at Measurement-Induced Transitions, Phys. Rev. Lett. **128**, 050602 (2022).
[45] A. Kumar, K. Aziz, A. Chakraborty, A. W. W. Ludwig, S. Gopalakrishnan, J. H. Pixley, and R. Vasseur, Boundary transfer matrix spectrum of measurement-induced transitions, Phys. Rev. B **109**, 014303 (2024).
[46] P. Hayden, S. Nezami, X.-L. Qi, N. Thomas, M. Walter, and Z. Yang, Holographic duality from random tensor networks, Journal of High Energy Physics **2016**, 9 (2016).
[47] R. Vasseur, A. C. Potter, Y.-Z. You, and A. W. W. Ludwig, Entanglement transitions from holographic random tensor networks, Phys. Rev. B **100**, 134203 (2019).
[48] C.-M. Jian, Y.-Z. You, R. Vasseur, and A. W. W. Ludwig, Measurement-induced criticality in random quantum circuits, Phys. Rev. B **101**, 104302 (2020).
[49] In a formulation using replicas, or any equivalent formulation that permits a description in terms of field theory, here specifically in terms of conformal field theory, that allows for a definition of a notion of central charge.
[50] P. Calabrese and J. Cardy, Entanglement entropy and quantum field theory, Journal of Statistical Mechanics: Theory and Experiment **2004**, P06002 (2004).
[51] P. Calabrese and J. Cardy, Entanglement entropy and conformal field theory, Journal of Physics A: Mathematical and Theoretical **42**, 504005 (2009).
[52] For the details of an explicit derivation of this type of expression see e.g. Ref. 23.
[53] A. W. Ludwig and J. L. Cardy, Perturbative evaluation of the conformal anomaly at new critical points with applications to random systems, Nuclear Physics B **285**, 687 (1987).
[54] J. Lykke Jacobsen and J. Cardy, Critical behaviour of random-bond Potts models: a transfer matrix study, Nuclear Physics B **515**, 701 (1998).
[55] A. Zabalo, M. J. Gullans, J. H. Wilson, R. Vasseur, A. W. W. Ludwig, S. Gopalakrishnan, D. A. Huse, and J. H. Pixley, Operator Scaling Dimensions and Multifractality at Measurement-Induced Transitions, Phys. Rev. Lett. **128**, 050602 (2022).
[56] J. L. Jacobsen and H. Saleur, Exact Valence Bond Entanglement Entropy and Probability Distribution in the XXX Spin Chain and the Potts Model, Phys. Rev. Lett. **100**, 087205 (2008).
[57] Y. Sasagawa, H. Ueda, J. Genzor, A. Gendiar, and T. Nishino, Entanglement Entropy on the Boundary of the Square-Lattice ±J Ising Model, Journal of the Physical Society of Japan **89**, 114005 (2020).
[58] A. B. Zamolodchikov, "Irreversibility" of the flux of the renormalization group in a 2D field theory, Soviet Journal of Experimental and Theoretical Physics Letters **43**, 730 (1986).
[59] R. Vasseur, J. L. Jacobsen, and H. Saleur, Universal Entanglement Crossover of Coupled Quantum Wires, Phys. Rev. Lett. **112**, 106601 (2014).
[60] B. Swingle, Entanglement does not generally decrease under renormalization, Journal of Statistical Mechanics: Theory and Experiment **2014**, P10041 (2014).
[61] D. Stauffer, Scaling theory of percolation clusters, Physics Reports **54**, 1 (1979).
[62] M. Hasenbusch, F. P. Toldin, A. Pelissetto, and E. Vicari, Critical and multicritical behavior of the ±J Ising model in two and three dimensions, Journal of Physics: Conference Series **145**, 012055 (2009).
[63] A. B. Harris, Effect of random defects on the critical behaviour of Ising models, Journal of Physics C: Solid State Physics **7**, 1671 (1974).
[64] J. T. Chayes, L. Chayes, D. S. Fisher, and T. Spencer, Finite-Size Scaling and Correlation Lengths for Disordered Systems, Phys. Rev. Lett. **57**, 2999 (1986).
[65] A. W. Ludwig, Infinite hierarchies of exponents in a diluted ferromagnet and their interpretation, Nuclear Physics B **330**, 639 (1990).
[66] S. Sang and T. H. Hsieh, Measurement-protected quantum phases, Phys. Rev. Research **3**, 023200 (2021).
[67] A. Lavasani, Y. Alavirad, and M. Barkeshli, Measurement-induced topological entanglement transitions in symmetric random quantum circuits, Nature Physics **17**, 342 (2021).
[68] J. Behrends, F. Venn, and B. Béri, Surface codes, quantum circuits, and entanglement phases, Phys. Rev. Res. **6**, 013137 (2024).
[69] P. Niroula, C. D. White, Q. Wang, S. Johri, D. Zhu, C. Monroe, C. Noel, and M. J. Gullans, Phase transition in magic with random quantum circuits, Nature Physics **20**, 1786 (2024).
[70] Z. Cheng, E. Huang, V. Khemani, M. J. Gullans, and M. Ippoliti, Emergent unitary designs for encoded qubits from coherent errors and syndrome measurements, arXiv e-prints 2412.04414.
[71] M. Pütz, R. Vasseur, A. W. W. Ludwig, S. Trebst, and G.-Y. Zhu, Data for "Flow to Nishimori universality in weakly monitored quantum circuits with qubit loss", Zenodo 10.5281/zenodo.15530142 (2025).

Supplementary notes

Appendix A: Analytical supplements

1. Gauge transformation

Here we show the gauge symmetry of the 2D tensor network allows us to relate different measurement outcomes $\mathbf{s} \to \mathbf{s}'$ with identical probability / partition function, see Fig. 7. In this way, we can fix a temporal gauge and restrict ourselves to the measurement outcomes that have straight vortex strings stretching across the spatial links, such that the corresponding (1+1)D deep circuit has a fixed X evolution gate, while the randomness occurs only to the ZZ evolution gates. Thus the (1+1)D deep circuit requires a post-selection of the X measurement outcomes, or by coupling the system to a bath with dissipation that leads to the imaginary time X evolution, with mid-circuit measurement of the ZZ operators. Note that our 2D quantum protocol does not need any (uniform) post-selection.

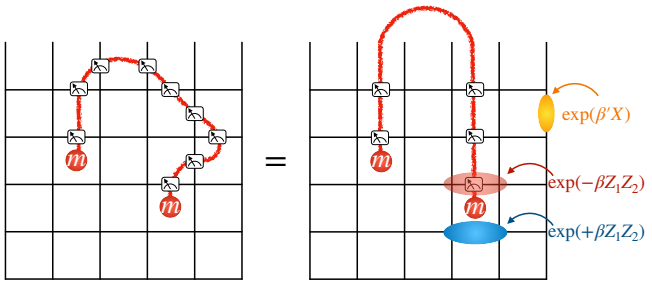

FIG. 7. **Gauge transformation**. We denote the negative measurement outcomes as a string (in red) passing by, along the dual lattice, whose end points define the m vortices. The gauge transformation can fluctuate the shape of the string, without altering the configuration of the m vortices. It relates two distinct measurement outcomes, with identical probability / partition function. The boundary 1+1D states are related by local Pauli X operators and thus share the same entanglement. As a result, we can always turn the string to be straight, such that the X evolution gate is fixed, while the randomness occurs only to the ZZ evolution gates.

2. Mixed state from measurement to noise channel

Here we provide more details on the last paragraph of the discussion section in main text by giving a more detailed derivation of the mixed state that arises after the measurement record is erased. First recall that the toric code under diluted weak measurement can be viewed [40] as a mixed state density matrix, by taking into account not only the system qubits of the toric code but also the auxiliary qubits that record the measurement outcome. This mixed state can be written as

$$\rho = \sum_{\mathbf{s}} |\mathbf{s}\rangle\langle\mathbf{s}| \otimes |\psi(\mathbf{s})\rangle\langle\psi(\mathbf{s})| \ , \tag{A1}$$

where $|\psi(\mathbf{s})\rangle$ is the un-normalized post-measurement wave function from Eq. (1) of the main text,

$$|\psi(\mathbf{s})\rangle = e^{\frac{\beta}{2}\sum_{\langle ij\rangle\in\mathcal{C}} s_{ij} Z_{ij}} |\psi_0\rangle \ .$$

Here, $|\psi_0\rangle = |\psi\rangle_{TC}$ is the initial perfect (unmeasured and undiluted) toric code state prior to the measurement, as the ground state of the star stabilizer operator $A_v = \prod_{\langle ij\rangle|v\in\partial\langle ij\rangle} Z_{ij}$ for any vertex v, and the plaquette stabilizer operator $B_p = \prod_{\langle ij\rangle\in\partial p} X_{ij}$ for any plaquette p (where ∂ denotes the boundary). The post-measurement state $|\psi(\mathbf{s})\rangle$, Eq. (1), is not an eigenstate of the plaquette operator B_p. Its norm yields the Born probability of each measurement outcome,

$$P(\mathbf{s}) = \langle\psi(\mathbf{s})|\psi(\mathbf{s})\rangle \ , \tag{A2}$$

which is related to the partition function of a random bond Ising model at inverse temperature $\beta = \tanh^{-1}\sin(2t)$ as defined in Eq. (2). From now on, we write more explicitly

$$P(\mathbf{s};\beta) \equiv P(\mathbf{s}) \tag{A3}$$

to emphasize the β dependence of the partition function. Here, the quantity $\mathbf{s}$ plays in the mixed state ρ of Eq. (A1) a role similar to a local "quantum number" that is conserved and specifies a block of the density matrix. Note that gauge equivalent configurations share the same probability: $P(\mathbf{s};\beta) = P(\mathbf{s}';\beta)$ if $\partial\mathbf{s} = \partial\mathbf{s}' = \mathbf{m}$, where we use $\partial\mathbf{s}$ to denote the end point configuration of the strings defined by $s_{ij} = -1$, as with the toric code convention, see Fig. 7 for an example. More concretely, we use $m_p = 1$ to label the existence of an excited m vortex on the plaquette p, and $m_p = 0$ otherwise, by defining $(-1)^{m_p} = \prod_{\langle ij\rangle\in p} s_{ij}$, the latter of which is usually called the Wilson loop operator in the gauge theory language. Thus one might as well label the probability function in Eq. (A3) by $P(\mathbf{m};\beta)$, bearing in mind that s recides on the bond center while m recides on the plaquette center. The bulk von Neumann entropy of the mixed state ρ in Eq. (A1) corresponds [40] to the Shannon entropy of the measurement record, $-\sum_{\mathbf{s}} P(\mathbf{s};\beta)\ln P(\mathbf{s};\beta)$, which is by Eq. (2) exactly the quenched free energy of the RBIM, since $P(\mathbf{s};\beta)$ can be interpreted as the disordered partition function. This establishes the map to the statistical model and the Nishimori transition point $t_c \approx 0.143\pi$ (Fig. 1 in the main text).

Now we show how the measurement problem can be related to the noise problem. If the measurement record is erased (i.e. traced out), the mixed state loses $\mathbf{s}$ as a good "quantum number", and is converted into

$$\tilde{\rho} = \mathrm{tr}_{\mathbf{s}}\rho = \sum_{\mathbf{s}} |\psi(\mathbf{s})\rangle\langle\psi(\mathbf{s})| = \prod_{\langle ij\rangle\in\mathcal{C}} \mathcal{N}_{ij}(|\psi_0\rangle\langle\psi_0|) \tag{A4}$$

where $\mathcal{N}_{ij}$ denotes a standard dephasing noise channel acting on a single bond qubit $\langle i,j\rangle$ as $\mathcal{N}_{ij}(|\psi_0\rangle\langle\psi_0|) = (1-\tilde{p})|\psi_0\rangle\langle\psi_0| + \tilde{p} Z_{ij}|\psi_0\rangle\langle\psi_0| Z_{ij}$. The effective noise probability $\tilde{p} = \sin^2(t)$ is obtained because on each single bond-qubit

$$\begin{aligned}\mathcal{N}_{ij}(|\psi_0\rangle\langle\psi_0|) &= \sum_{s_{ij}=\pm 1} e^{\beta s_{ij} Z_{ij}/2} |\psi_0\rangle\langle\psi_0| e^{-\beta s_{ij} Z_{ij}/2} \\ &= \cos^2(t)|\psi_0\rangle\langle\psi_0| + \sin^2(t) Z_{ij}|\psi_0\rangle\langle\psi_0| Z_{ij} \ .\end{aligned} \tag{A5}$$

In this way, the weak measurement limit $t = 0$ corresponds to the noiseless and the projective measurement limit $t = \pi/4$ corresponds to the maximally noisy limit. Since the Kraus operator Z_{ij} (at each bond $\langle i,j\rangle$) acts on both sides of the density matrix, the m (anyon) vortex of the toric code is a conserved quantity and serves as the local "quantum number" that replaces the aforementioned quantity $\mathbf{s}$. The mixed state becomes, after tracing out the measurement record, a grand canonical ensemble of the m vortices,

$$\tilde{\rho} = \sum_{\mathbf{m}} P(\mathbf{m};\tilde{\beta}) \left|\tilde{\psi}(\mathbf{m})\right\rangle\!\left\langle\tilde{\psi}(\mathbf{m})\right| \tag{A6}$$

where $\left|\tilde{\psi}(\mathbf{m})\right\rangle$ now denotes a *normalized* random toric code eigenstate with eigenvalue $B_p = (-1)^{m_p}$ and $\mathbf{m}$ labels an arbitrary configuration of the m vortices distributed in space. The probability distribution of each such $\mathbf{m}$ configuration is given by Ref. [1]:

$$P(\mathbf{m};\tilde{\beta}) \propto \sum_{\mathbf{s}|\partial\mathbf{s}=\mathbf{m}} \left(\frac{p}{1-p}\right)^{\sum_{ij}\frac{1-s_{ij}}{2}} \propto \sum_{\sigma} e^{\tilde{\beta}\sum_{\langle ij\rangle} s_{ij}\sigma_i\sigma_j} . \tag{A7}$$

As a partition function, it collects the weights of all possible error chains of Pauli Z_{ij} operators on bonds $\langle i,j\rangle$, supported on the string path that ends at the m vortices, which is, strictly along the Nishimori line $\tilde{p}/(1-\tilde{p}) = e^{-2\tilde{\beta}}$, dual to the partition function of the random bond Ising model. To summarize, the noisy mixed state $\tilde{\rho}$ is mapped to the RBIM along the Nishimori line described by the partition function $P(\mathbf{m};\tilde{\beta})$, with disorder probability $\tilde{p} = \sin^2(t)$ and inverse temperature $\tilde{\beta} = \tanh^{-1}\cos(2t)$.

For comparison, the measurement induced mixed state (A1), thus containing the measurement record $|\mathbf{s}\rangle\langle\mathbf{s}|$, is mapped to the RBIM along the Nishimori line described by partition function $P(\mathbf{s})$ with disorder probability $p = \cos^2(t)$ and temperature $\beta = \tanh^{-1}\sin(2t)$ in Ref. [2]. Note the crucial fact that $\tilde{\beta}$ is the Kramers-Wannier dual of β: $\tilde{\beta} = -\frac{1}{2}\ln\tanh\beta$. Namely, erasing the measurement record effectively induces a high temperature to low temperature duality, reversing the temperature of the effective statistical model along the Nishimori line. Besides, it also turns the non-stabilizer state $|\psi(\mathbf{s})\rangle$ into a stabilizer state $\left|\tilde{\psi}(\mathbf{m})\right\rangle$.

In the absence of dilution, despite the microscopic difference, both the post-measurement states ρ and the noisy states $\tilde{\rho}$ are described by Nishimori criticality. In the presence of dilution, only a finite fraction of the qubits, supported on the bonds $\langle ij\rangle \in \mathcal{C}$, are subjected to measurement in ρ and dephasing in $\tilde{\rho}$. Here the volume of the support $|\mathcal{C}| = p_{meas}N_B$ is a fraction of the total number of bonds N_B under a fixed probability p_{meas}. Note the crucial fact that this probability p_{meas} plays a different role than $\tilde{p}$ in the dephasing case, because the dilution is a so-called "heralded" or "flagged" error, which means the information $\mathcal{C}$ is known. In contrast, in Eq. (A5), one does not have a "flag" when Z_{ij} is applied. The global phase diagram for such a scenario is left for future study. Nonetheless, at $t = \pi/4$, the percolation transition at 50% still holds. Therefore, in such noise phase diagram, there is still a critical line between the exact Nishimori transition at $t = 0.107\pi$ and the exact percolation transition at 50%, see Fig. 6. We expect the same RG flow between these two critical points.

3. Coherent information / domain wall entropy

In technical terms, the coherent information for every post-measurement pure state is given by the measurement (disorder) average of the domain-wall entropy

$$I_{\mathbf{s}} = -\frac{1+C_{\mathbf{s}}}{2}\log_2\frac{1+C_{\mathbf{s}}}{2} - \frac{1-C_{\mathbf{s}}}{2}\log_2\frac{1-C_{\mathbf{s}}}{2} , \tag{A8}$$

where $C_{\mathbf{s}}$ the overlap between the two topologically degenerate states of the surface code conditioned upon a given measurement record $\mathbf{s}$. In the dual Ising representation, C is the correlation between two test spins placed on the left and right boundaries of the lattice [2]. The left (right) test spin interacts with all qubits on the left (right) boundary with the same Ising interaction strength, also subjected to the bond randomness. Consequently, C can be viewed as the expectation value of a "domain wall" operator (with eigenvalue ±1):

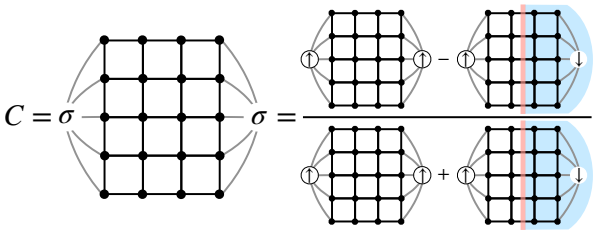

, (A9)

conditioned upon a given measurement record $\mathbf{s}$. Using the typical scaling dimension of the domain wall operator Δ_m, we should find the typical asymptotic behavior of C when $L_y \gg L_x$ for a fixed disorder realization:

$$C_{\mathbf{s}} \sim \frac{1 - e^{-2\pi\Delta_m\frac{L_y}{L_x}} + \cdots}{1 + e^{-2\pi\Delta_m\frac{L_y}{L_x}} + \cdots} = \tanh\left(\pi\Delta_m\frac{L_y}{L_x}\right) + \cdots , \tag{A10}$$

which gives a partial explanation why the domain wall entropy at the critical point does not scale with the system size, once the aspect ratio L_y/L_x is fixed. Note that this is analogous to using the domain wall energy as scaling invariant probe for the Nishimori critical point at the long cylinder limit [42, 43].

4. Multifractality

In this appendix, we briefly review the multifractal nature of entanglement entropies at measurement-induced phase transitions, following Refs. [23, 55] and the earlier work in Ref. [65]. The key observation is that the quantity

$$G_n(x_1,x_2,\mathbf{s}) = \mathrm{tr}(\rho(\mathbf{s}))^n = e^{-(n-1)S_n(\mathbf{s})}, \tag{A11}$$

with $A = [x_1,x_2]$ parametrizing the entanglement interval, defined for a fixed quantum trajectory "s", behaves as a two-point correlation function in a disordered medium (due to the

method	tensor networks			Clifford simulations	free-fermion network
Observable	I_c		S_n	S_n	S_n
largest system size $L_x \times L_y$	257×256	513×512	1024×2048	1024×4096	$1024 \times 20480^*$
# of data points	300	20	15	1	1
# of samples / data point	100,000	100,000	50,000	14,400,000	18,000,000
# of total core hours	650,000	350,000	150,000	200,000	2,300,000
total file size	1.3 GB	15 MB	60 GB	220 GB	2 TB

TABLE II. **Computational resources.** To characterize the computational effort for our numerical simulations we provide, for the largest system sizes that we have simulated, the number of data points sweeping the phase diagram, number of samples per data point, the total number of core hours, and typical data storage requirements for simulations using the numerical techniques indicated at the top of every column. The first column lists the numbers for the tensor network simulations of the coherent information I_c throughout the phase diagram. This data is used to calculate the location of the critical line connecting the percolation point and the Nishimori point, as well as determining the critical exponent ν along that critical line (see Fig. 3). Limited to the Nishimori line, we do the same simulation for larger system sizes (second column). We use the tensor network method to calculate the entanglement entropies S_n at different points along the critical line in open boundary conditions (third column). This data is used to determine the effective central charge $c_{\rm ent}$ along the critical line (see Fig. 2) to see the crossover behavior between percolation and Nishimori criticality. In order to calculate the entanglement entropy in periodic (and open) boundary conditions much more efficiently at the percolation point, we use Clifford simulations (fourth column). This data is used to determine the cumulants shown in Fig. 4(a) and 10(a). Similarly, we use free-fermion network evolution to calculate the entanglement entropies in periodic boundary conditions at the Nishimori point (fifth column). The asterisk (*) indicates, that we calculate the entanglement entropies multiple times while evolving the 1D quantum state, starting after a thermalization time of 4096 time steps. The data is used to determine the cumulants for the Nishimori point, shown in Figs. 4(b), 5, 10(b) and 11.

random nature of the measurement outcomes). More precisely, this is the two-point function of a boundary-condition changing (bcc) operator in the associated CFT [47, 48]. Upon averaging over measurement outcomes, different powers of this correlator can scale at criticality with exponents which are entirely independent universal numbers for different values of the moment order k [65],

$$\overline{\left(G_n(x_1,x_2,\mathbf{s})\right)^k} = \overline{e^{-k(n-1)S_n(\mathbf{s})}} \propto R^{-2X_{n,k}}, \qquad \text{(A12)}$$

where we recall that the overbar denotes the average with respect to the Born rule probability distribution for the measurement outcomes "$(\mathbf{s})$". If this happens the scaling is referred to as "multifractal", and in the present context such scaling occurs for the quantity in Eq. (A12). Importantly, because the origin of this infinite hierarchy of independent critical exponents is a universal scaling form [65] of the entire probability distribution of the random variable $G_n(x_1,x_2,\mathbf{s})$, the scaling dimensions $X_{n,k}$ can be defined for general real indices n and k, and thus define a continuum of scaling dimensions.

In practice, it is more convenient numerically to work with self-averaging quantities such as the Rényi entropies $S_n(\mathbf{s})$ as opposed to the quantity in Eq. (A11). The consequences of the multifractal scaling (A12) for Renyi entropies can be derived by performing a *cumulant expansion* of $\overline{e^{-k(n-1)S_n(\mathbf{s})}}$ and Taylor expanding $R^{-2X_{n,k}}$ in the moment order 'k'. Focusing on the 2nd Rényi entropy ($n = 2$) for simplicity, we have

$$\overline{e^{-kS_2(\mathbf{s})}} = \exp\left(-k\kappa_1 + \frac{k^2}{2!}\kappa_2 - \frac{k^3}{3!}\kappa_3 + \dots\right), \qquad \text{(A13)}$$

with the cumulants defined in Eq. (9). Now if we Taylor expand the scaling dimension $X_{2,k} = \sum_m \frac{x_2^{(m)}}{m!}k^m$, we have

$$R^{-2X_{n,k}} = \exp\left(-2\left[kx_n^{(1)} + \frac{k^2}{2!}x_n^{(2)} + \dots\right]\ln R\right) \qquad \text{(A14)}$$

with $n = 2$. Comparing the latter two equations, we find in view of Eq. (A12) the following scaling of all cumulants of the 2nd Rényi entropy

$$\kappa_m \sim 2(-1)^{m-1}x_2^{(m)}\ln R, \qquad \text{(A15)}$$

which is the relation used in the main text. An analogous result is arrived at for general $n > 1$. Because the density matrix $\rho(\mathbf{s})$ appearing in Eq. (A11) is *normalized*, a trivial result is obtained for the direct $n \to 1$ limit of the moment exponents $X_{n,k}$.

Appendix B: Supplementary numerical data

1. Computational costs

Our numerical codes have been run on national high-performance computing resources, specifically the AMD EPYC (v3 Milan)-based Noctua2 cluster at the Paderborn Center for Parallel Computing (PC2), the AMD EPYC (v4 Genoa)-based RAMSES cluster at RRZK/University of Cologne, and the Intel XEON Platinum 8168-based JUWELS cluster at FZ Julich. An overview of key characteristics for production runs on these machines is provided in Table II above.

2. Entanglement peak location

One particular striking numerical result presented in the main text is the non-monotonous behavior of the effective central charge estimate $c_{\rm ent}$ along the RG flow from percolation to Nishimori shown in Fig. 2 of the main text. Since we show data for different system sizes $L = 64, 128, 256, 512, 1024$ one

might ask for a finite-size extrapolation of this data, which we present here.

In Fig. 9 below, we show how the peak position for increasing system sizes moves towards the percolation fixed point ($\theta = \pi/2$), with panel (a) showing θ_{peak} as a function of inverse system size, while panel (b) shows the distance of θ_{peak} from the percolation fixed point as a function of inverse system size in a doubly logarithmic plot. The latter data falls on top of a line, indicating a power-law fit (dashed line), indicating that peak position indeed moves to the percolation limit for infinite system size $L \to \infty$. Physically, this implies a step-function behavior in the thermodynamic limit where upon moving away from the Clifford-limit of percolation the system immediately picks up a seizable amount of entanglement (available from spreading the Clifford-constrained wavefunction to the fully available Hilbert space).

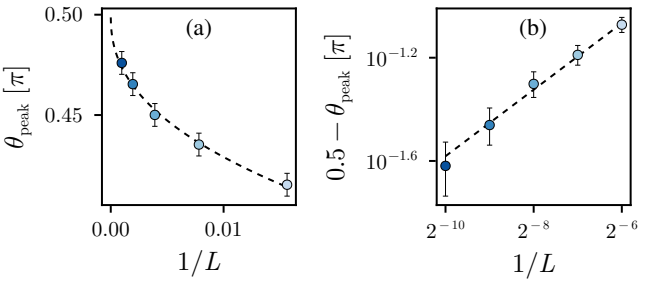

FIG. 9. **Entanglement peak location**. To extrapolate the peak position of c_{ent} to the thermodynamic limit $L \to \infty$, we show (a) θ_{peak} (determined from the data in Fig. 2) against the inverse system size, and (b) its distance from $\pi/2$ versus inverse system size on a doubly-logarithmic scale. We fit the power law function $f(x) = p_1 x^{p_2}$ to the data. The optimal coefficients are $p_1 = 0.509(53)\pi$ and $p_2 = 0.428(21)$.

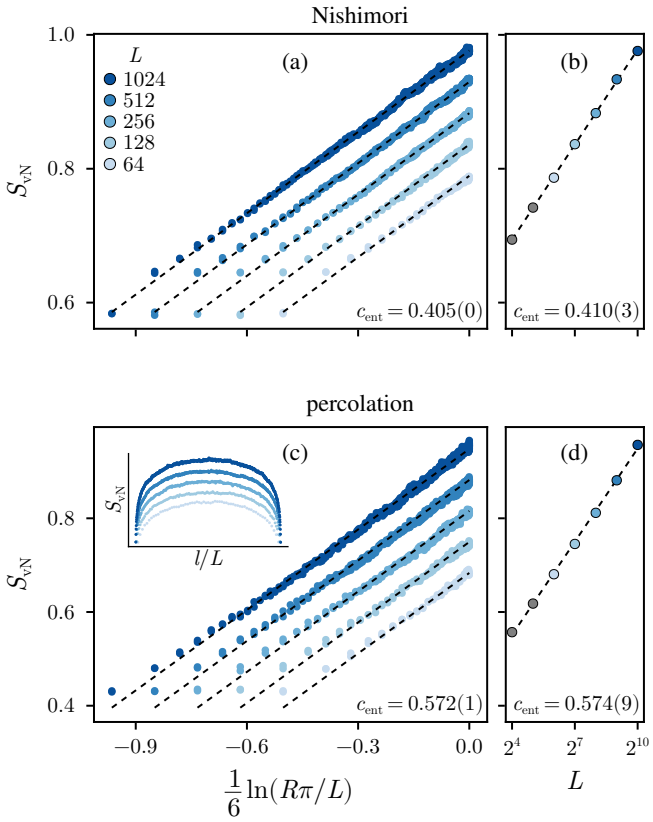

FIG. 8. **Entanglement scaling: Nishimori point (top panel) versus percolation point (bottom panel).** Left panel: effective central charge fit by the variation of entropy with *varying entanglement cut*: $S_{\text{vN}}(l) - S_{\text{vN}}(l = L/2)$ as a function of l/L. We fit one slope for all system sizes. Right panel: the effective central charge is fit to the scaling of the *half-cut* entanglement entropy with the system size: $S_{\text{vN}}(l = L/2)$ as a function of L. For the computation a long stripe $L_y = 2L_x = 2L$ is chosen to guarantee the boundary 1D quantum state reaches steady state of the transfer matrix. The boundary condition is open boundary. The MPS cutoff is set to 10^{-20}.

3. Numerical estimation of cumulants

Figs. 10 and 11 provide a detailed account of our data fitting procedure to extract the leading five cumulants from fits to the entanglement entropy for the system sizes up to $N = 1024 \times 4096$ using periodic boundary conditions.

Nishimori versus percolation criticality

Concentrating first on the data in Fig. 10 one can see that the Nishimori universality class leads to cleaner data than percolation criticality, which one might rationalize by the fact that the percolation/Clifford problem is obtained from averaging *discrete* data, which requires more samples to converge.

For both universality classes, the "arc structure" of the entanglement entropy, when plotted as a function of subsystem size l/L, is clearly visible (as demanded by the analytical form of Eq. 5) and switches its overall sign for the fourth-order cumulant (as expected analytically for percolation, but unknown in the case of Nishimori universality).

When trying to fit the fourth order cumulant, we note that this is a challenging task for the percolation data. In fact, there is a strong dependence of the numerical estimate of the cumulant when restricting the data set to only fit the bulk data in the middle of the arc. What an ideal choice might look like is not at all obvious and we have "cherry-picked" the interval to obtain an estimate close to the analytical prediction (which, of course, does not serve as an independent confirmation anymore). In contrast, there is no such need for outside guidance for the case of Nishimori criticality where we can provide a high-precision estimate for the fourth-order cumulant from following the same fitting protocol as for all other cumulants. We can even expand this approach to obtain an estimate for the fifth-order cumulant, as shown in the lower right panel of Fig. 10, though the fit is clearly of much lesser quality than the other cumulants.

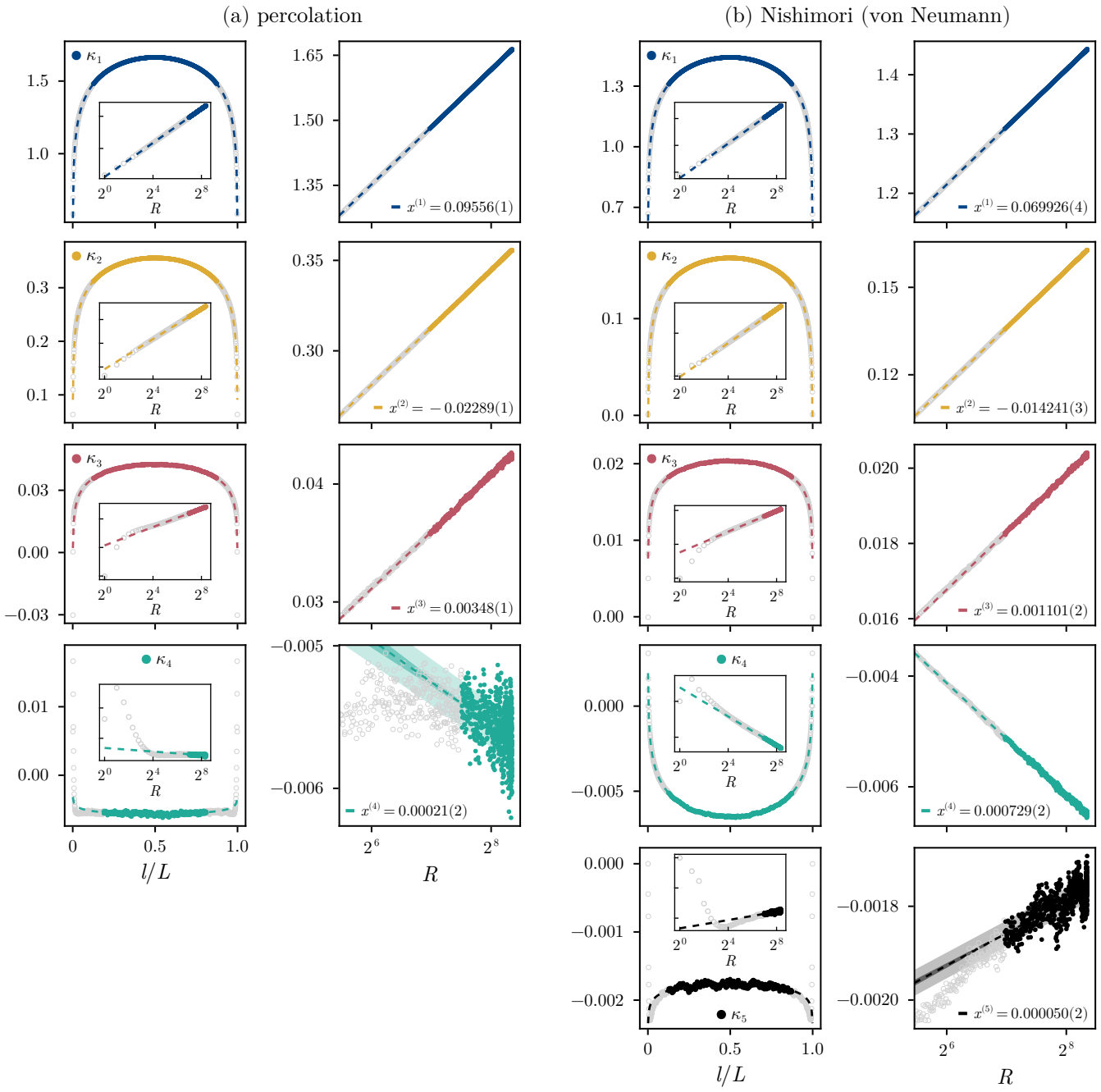

FIG. 10. **Multifractality and cumulants (periodic boundary conditions).** Left panels: percolation criticality. Right panels: Nishimori criticality. The underlying data is for the von Neumann entropy of system sizes $L = 1024$ using *periodic* boundary conditions. Data is averaged over $\sim 14,000,000$ (percolation) and $\sim 18,000,000$ (Nishimori) samples. For percolation we employed Clifford simulations, while for Nishimori universality we used free fermion simulations (see main text).

Higher-order Rényi entropies

Notably, the quality of the cumulant fits further improves as one goes from the $n = 1$ von Neumann entropy to higher-order Rényi entropies, with a direct comparison shown in Fig. 11 for the second and $n = \infty$ Rényi entropies. Of particular interest might be the behavior of the fifth-order cumulant, which exhibits a sign change when going from the first to second Rényi entropy (and then remains negative for all higher-order Rényi entropies).

Boundary conditions

Let us close with the observation that, in our simulations, *periodic* boundary conditions (see, e.g., Fig. 10) lead to much

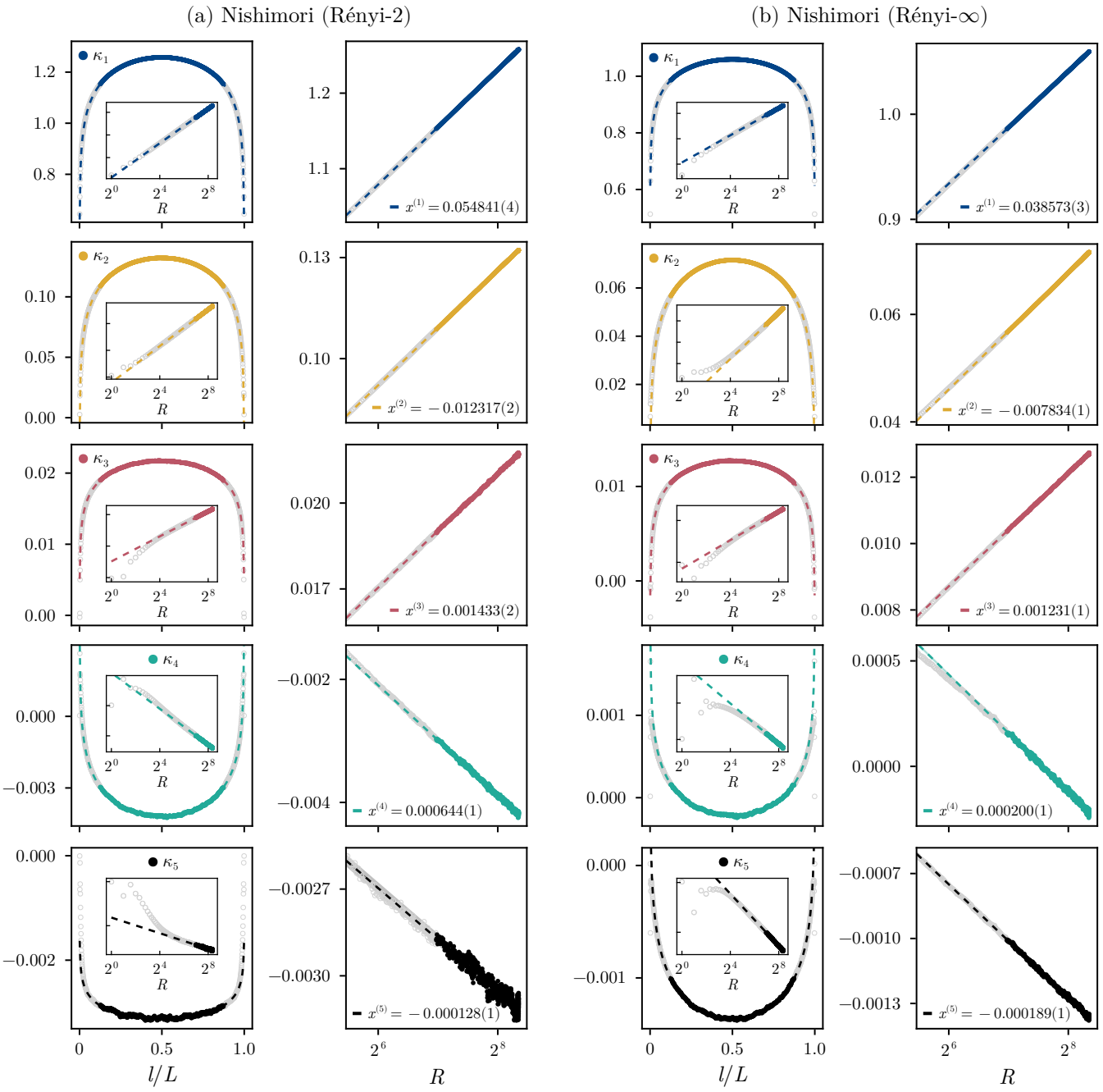

FIG. 11. **Multifractality and cumulants for higher-order Rényi entropies (periodic boundary conditions).** Same as Fig. 10 but for the second Rényi entropy (left) and $n = \infty$ Rényi entropy (right). Data is again for system sizes $L = 1024$ averaged over $\sim 18,000,000$ samples. Note that the fifth cumulant switches sign when going from SvN [Fig. 10(b)] to the higher-order Rényi entropies.

cleaner data than *open* boundary conditions (Fig. 12). This might be a useful pointer for any future calculations of cumulant estimators.

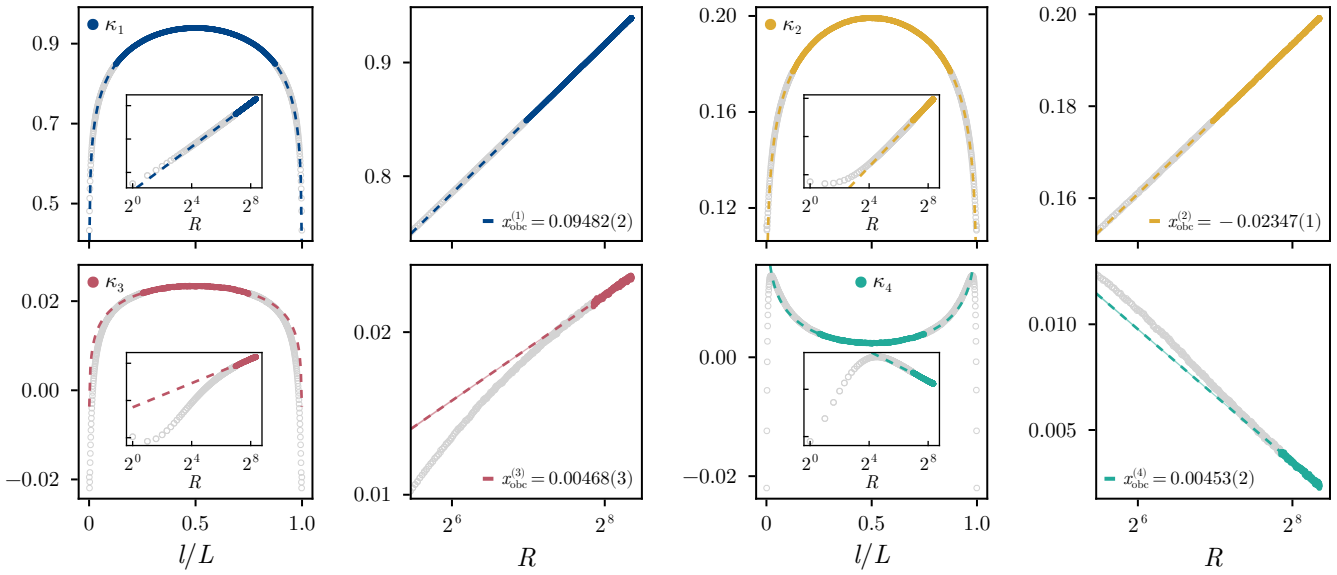

FIG. 12. **Multifractality and cumulants for percolation (open boundary conditions).** The underlying data is for the von Neumann entropy of system sizes $L = 1024$ using *open* boundary conditions. Data is calculated using Clifford simulations and averaged over $\sim 14,000,000$ samples. Note that, starting from the third cumulant, we observe boundary effects that further increase for the fourth cumulant, cf. Fig. 10(a) where such effects are absent for *periodic* boundary conditions. To minimize such boundary effects on third and fourth cumulant estimates we only fit half of the data points in the bulk.